Small Structures

small structures

www.small-structures.com

RESEARCH ARTICLE OPEN ACCESS

Confined Chemistry in Space: Zeolite-Supported Fe_{13} Nanoclusters Modulate CS Reactivity

Gerard Pareras[1] | Albert Rimola[1,2]

[1]Departament de Química, Universitat Autònoma de Barcelona, Bellaterra, Spain | [2]Accademia delle Scienze di Torino, Torino, Italy

Correspondence: Gerard Pareras (gerard.pareras@uab.cat) | Albert Rimola (albert.rimola@uab.cat)

Received: 23 December 2025 | **Revised:** 6 February 2026 | **Accepted:** 6 February 2026

Keywords: astrochemistry | chabazite | DFT | Fe nanoclusters | zeolite-confined catalysis

ABSTRACT

Zeolites are plausible nanoreactors in astrochemical environments, where their internal porosity and ability to host transition metals modulate surface reactivity under near-vacuum conditions. We investigate the confined chemistry of carbon monosulfide (CS) and hydrogen (H_2) on an Fe_{13} nanocluster embedded in chabazite (Fe_{13}@CHA) using density functional theory and microkinetic modeling. Motivated by the long-standing "missing sulfur" problem and the relevance of thioformaldehyde (H_2CS), we use CS + H_2 as a test reaction. On Fe_{13}@CHA, H_2 dissociates and CS adsorption strongly polarizes the C—S bond; confinement tilts the competition between pathways so that C—S bond scission dominates over H_2 addition toward H_2CS. The resulting C and S adatoms are trapped and funnel reactivity toward H_2S and CH_4 via sequential hydrogenation. Calculations on an open Fe_{13}@SiO_2 surface show that, in the absence of confinement, CS hydrogenation to HCS is preferred, confirming that the shift in chemoselectivity is a genuine confinement effect. Insertion of a second CS molecule (without H_2) enables the formation of CS_2, C_2S, and C_2 species, with barriers that favor C–C over S–S coupling. Kinetic analysis indicates that these processes become efficient at mid-to-high temperatures, identifying inner protoplanetary regions as promising environments where zeolitic grains sequester sulfur and reshape CS-based chemistry.

1 | Introduction

Zeolites are crystalline, sponge-like aluminosilicates with perfectly uniform, molecular-scale pores that turn them into tiny chemical factories. Although minerals such as faujasite, mordenite, and chabazite are found in nature, it was the rise of synthetic zeolites in the mid-20th century that revealed their catalytic power, most famously in fluid catalytic cracking, which reshaped fuel production. What makes zeolites special is not only their acidity but also shape selectivity: Pores and cages allow certain molecules to pass while blocking others, and they influence transition-state dimensions to guide reactions with high precision. From upgrading petroleum to tailoring petrochemicals, zeolites show how geometry, composition, and topology can be engineered to control reactivity, atom by atom and Angstrom by Angstrom [1–7].

Beyond refineries, zeolites matter in space science because they are plausible minerals in other planets also acting as powerful nanoreactors. Orbital and spectral studies suggest zeolitic phases in Martian dust and altered basalts, and several groups have proposed that chabazite/clinoptilolite in the Martian subsurface could trap and episodically release methane, offering an alternative to clathrate reservoirs [8–12]. From an astrochemical perspective, zeolites are compelling because confinement effects, the way how pores and cages preorganize molecules and transition states, can tilt reaction pathways without changing stoichiometry. Work across heterogeneous catalysis shows that micro- and nanoporous confinement can lower energy barriers, alter entropies and redirect selectivity [13–16]. Accordingly, the same principles can apply in astrophysical environments, from early interstellar and circumstellar media (regions between and around nascent stars, rich in nm–mm dust grain particles) to planet forming regions, in which dust aggregates coalesce forming first pebbles and later planetesimals, eventually converting into planets, or alternatively in comets, meteorites, and other

asteroidal bodies. The presence of such dust particles, which can present porosity of different degrees, can indeed be active in mineral microreactors relevant to astrochemistry and prebiotic chemistry. Moreover, meteorites record extensive aqueous alteration on early Solar System bodies, which are propitious conditions under which zeolites form, highlighting their relevance as porous, gas-sorbing systems in cosmic environments [17].

Porosity is particularly important under the near-vacuum conditions characteristic of astrophysical environments: Zeolitic cages act as nanoreactors that locally concentrate reactants, protect reactive intermediates, and enhance effective reactivity. Crucially, zeolites can also host transition metals. This links to the long-standing "missing iron" problem: Despite the relatively high cosmic abundance of elemental iron, observations show a deficit in the gas phase, implying sequestration into dust as lattice substitutions, adatoms, or nanoclusters [18–23]. In this sense, zeolite pores provide a credible reservoir for Fe in small aggregates, enabling a dual synergy that is uncommon in astrochemical models: the catalytic properties of transition metals combined with the confinement effects within molecular-sized pores.

Transition-metal-driven catalysis in astrochemistry has gained momentum over the last decade. There is growing evidence that Fischer–Tropsch-type (FTT) chemistry can proceed on cosmic mineral surfaces under astrophysical inspired conditions, with Fe-bearing materials playing a crucial role. Yet, direct H_2–CO coupling faces substantial energetic bottlenecks: Mechanistic studies indicate high activation barriers for key steps, restricting efficient conversion to environments where additional energy inputs are available, thus rendering rates negligible in the coldest regions of the interstellar medium (ISM, typically $T < 100$ K) [24–30]. This motivates exploring nanoconfinement as a way to reshape the free-energy landscape of surface reactions.

Within this context, our aim is to explore ways to overcome the current bottlenecks by introducing two shifts to the prevailing space FTT paradigm. First, we employ the, chabazite zeolite as a support for an Fe_{13} nanocluster, using its cages and eight-ring windows as nanoreactors that gather and preorganize reactants. Second, we leverage the metal cluster to tune the reaction landscape under confinement, since reactions in nanoporous environments can reshape mechanisms and barriers. As a concrete testbed, we will examine the hydrogenation of CS by H_2 toward thioformaldehyde (H_2CS). This choice speaks directly to the long-standing puzzle of sulfur chemistry in interstellar environments: While the observed sulfur abundance in diffuse ISM is near the cosmic value ($S/H \approx 1.3–1.5 \times 10^{-5}$), in denser ISM regions, gas sulfur is strongly depleted ($\sim$0.1% of cosmic abundance detected in the gas phase), its dominant reservoirs remaining uncertain [31–42]. Despite extensive work on sulfur chemistry networks, direct H_2-driven hydrogenation of CS to H_2CS under space-relevant conditions has been less explored. Here, we propose that confined chemistry can concentrate reactants, protect intermediates, and modulate transition states, thereby funneling reactivity in ways not available on open dust surfaces. By combining Fe nanocatalysis with zeolitic confinement, we seek to establish a mechanistic basis for CS to H_2CS conversion in astrochemical settings and to assess whether trapping of CS and its reactivity with H_2 inside CHA could shed light on the broader missing sulfur problem.

2 | Results

Upon construction of the Fe_{13}@CHA catalyst, the reaction proposed here to study is the direct H_2–CS coupling to obtain thioformaldehyde (Figure 1, Rx. 1). Interestingly, the CS molecule can also undergo C—S bond cleavage upon interaction with the metal cluster, yielding separate C and S adatoms (Figure 1, Rx. 2). This process will also be evaluated, followed by subsequent H_2 addition to the newly formed S atom to form H_2S (Figure 1, Rx. 3), as well as double H_2 addition to the newly formed C atom forming first CH_2 and later CH_4 (Figure 1, Rx. 4).

Figure 2 shows the potential energy surface (PES) for the H_2 addition to CS (Figure 1, Rx. 1) and the C–S cleavage of CS upon adsorption (Figure 1, Rx. 2). The sequence initiates with the H_2 adsorption on the Fe_{13}@CHA surface, leading to a barrierless H_2 cleavage on the metal cluster (consistent with previous work using Fe_{13}@SiO_2 as catalyst) [27]. This delivers two H atoms (Figure 2, structure B), the electronic analysis of which indicating a homolytic process (each H holding one electron). Subsequently, adsorption of CS to Fe_{13}@CHA polarizes the C—S bond, with an elongation of 0.16 Å (Figure 2, structure C) and thus weakening it, mirroring what was reported for CO [27]. From this structure C, both the hydrogenation of CS and the CS bond cleavage have been evaluated. Calculated PESs indicate close competition between the two processes: The intrinsic barrier for the hydrogenation is 21.9 kcal mol^{-1}, whereas that for the C–S cleavage is 24.7 kcal mol^{-1}. Interestingly, the HCS intermediate exhibits a pronounced elongation of the C—S bond, from 1.70 Å in CS to 1.91 Å (Figure 2, structure D*), which is beyond the typical C–S single-bond lengths, indicating an almost negligible C–S chemical bond. That is, the hydrogenation of CS under CHA confinement induces the CS bond cleavage, which can explain why the two barriers present similar heights.

To check upon this point, we also examined the interaction between the H–C and the S moieties in structure D*. NEB calculations show a monotonic increase in the H–C···S separation toward a more stable, fully dissociated arrangement, without an intervening saddle point (Figure 2). The global minimum reached after the putative HCS stage is structure D in Figure 2, in which HC and S are completely separated. This dissociation is strongly exergonic, with a final relative energy of −78.5 kcal mol^{-1}, confirming that C—S bond cleavage is the favored path over formation of HCS. Accordingly, H_2CS formation via hydrogenation of HCS can be ruled out.

For consistency, we also examined the same CS hydrogenation pathway on the Fe_{13}@SiO_2 model catalyst from our previous FTT studies [27]. The corresponding energies and structures are reported in Table S1 and Figure S1. In the absence of CHA confinement, the reaction proceeds through CS hydrogenation toward HCS. Moreover, the optimized HCS product shows a C—S bond length of 1.784 Å, within the typical C—S bonding range. These complementary calculations therefore support that

$$CS + H_2 \longrightarrow H_2CS \quad \text{Rx. 1}$$

$$CS \longrightarrow C + S \quad \text{Rx. 2}$$

$$S + H_2 \longrightarrow H_2S \quad \text{Rx. 3}$$

$$C + H_2 \longrightarrow CH_2 + H_2 \longrightarrow CH_4 \quad \text{Rx. 4}$$

FIGURE 1 | Reactions proposed in the present work.

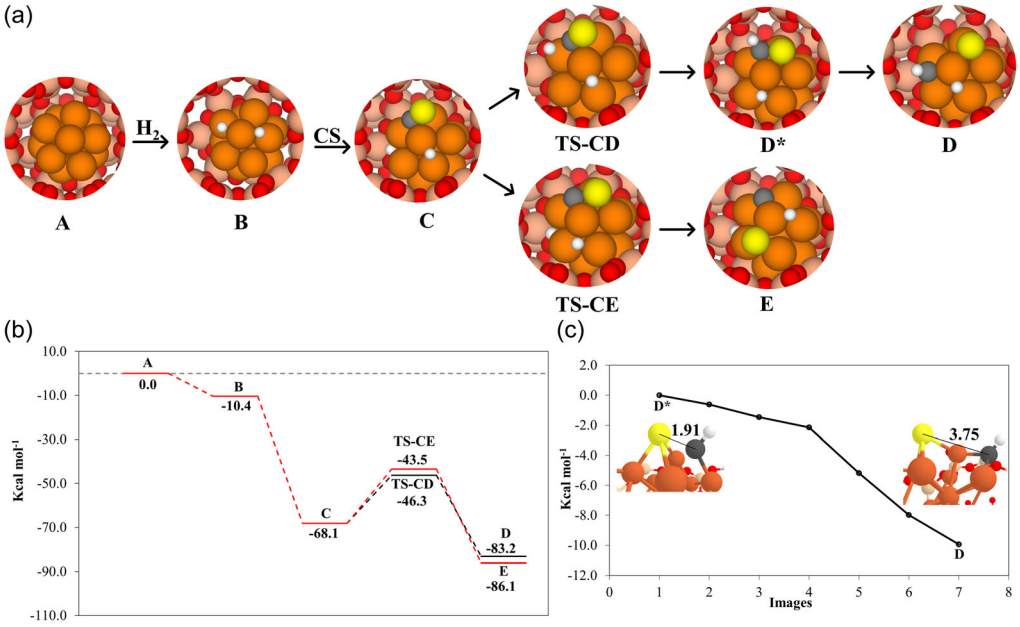

FIGURE 2 | (a) Optimized structures and transition state structures for the reaction processes for the hydrogenation of CS and the direct cleavage of the CS bond. (b) Potential energy surface for the hydrogenation process (black) and the direct cleavage of CS (red). (c) NEB plotted energies from the transition between D^* and D. Included the optimized structures upon hydrogenation of the CS moiety. D^* is the immediate optimized structure upon the hydrogenation, and D is the final separated HC–S moieties. Energies are in kcal mol^{-1}. Distances are depicted in Angstroms (Å). Color coding: white, H atoms; red, O atoms; beige, Si atoms; orange, Fe atoms; gray, C atoms; and yellow, S atoms.

the change in chemoselectivity observed on Fe_{13}@CHA is a genuine confinement effect.

At this point, the network branches into three channels: (i) S-centered hydrogenation to form H_2S, (ii) C-centered hydrogenation to form CH_2, and (iii) HC-centered hydrogenation to form CH_2. However, it is worth mentioning that for case (ii), once C has been hydrogenated by one H atom, it forms CH, moving to the HC-centered hydrogenation, namely, case (iii). Moreover, these two latter processes can be followed by a new H_2 addition to form CH_4.

Figure 3 shows the H_2S formation channel. The first H addition to sulfur presents a barrier of 51.4 kcal mol^{-1} yielding HS in an endergonic elementary step, while the second H addition proceeds through an overall energy barrier of 62.2 kcal mol^{-1} to produce H_2S, with the final product being endergonic with respect to the initial reactants.

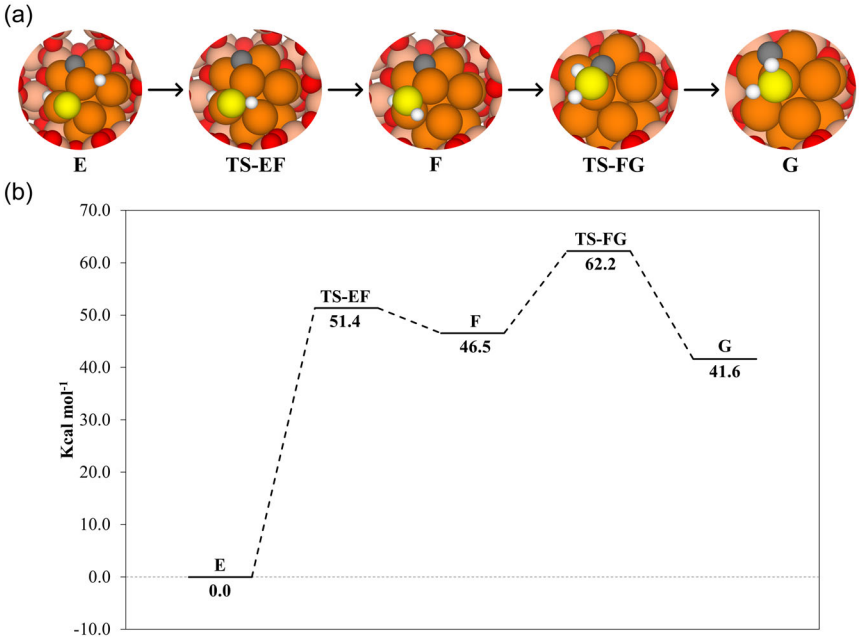

FIGURE 3 | (a) Optimized structures and transition state structures for the reaction processes for the hydrogenation of S to form H_2S. (b) Potential energy surface for the hydrogenation process. Energies are in kcal mol^{-1}. Color coding: white, H atoms; red, O atoms; beige, Si atoms; orange, Fe atoms; gray, C atoms; and yellow, S atoms.

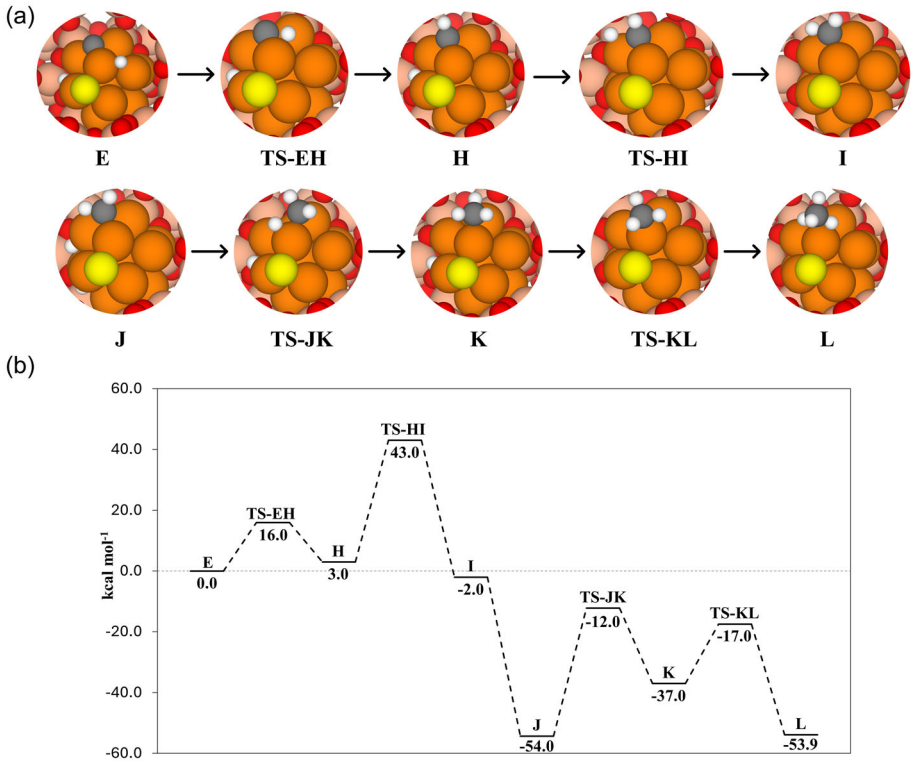

FIGURE 4 | (a) Optimized structures and transition state structures for the reaction processes for the hydrogenation of C to form CH_4. (b) Potential energy surface for the hydrogenation process. Energies are in kcal mol^{-1}. Color coding: white, H atoms; red, O atoms; beige, Si atoms; orange, Fe atoms; gray, C atoms; and yellow, S atoms.

The carbon-hydrogenation sequence, first to CH_2 and then to CH_4, proceeds via a mechanism analogous to H_2S formation. The PES in Figure 4 shows that hydrogenation of C to give CH presents a barrier of 16.0 kcal mol^{-1} and the subsequent hydrogenation to CH_2 requires a higher barrier of 43.0 kcal mol^{-1}, in which CH formation is slightly endergonic, whereas CH_2 formation is slightly exergonic. Insertion of a second H_2 molecule again yields the homolytic dissociation of the molecules, forming a highly stable intermediate (structure J of Figure 4). Formation of CH_3 proceeds through intrinsic energy barriers (i.e., with respect to intermediate J) of 42.1 and 37 kcal mol^{-1} for the first and second hydrogenations, respectively, forming CH_3 in an endergonic way and the final CH_4 with a similar stability as J.

In summary, this mechanistic analysis shows that CS does not evolve to H_2CS via H_2 addition; instead, it cleaves to S and C (or CH). However, further hydrogenations of S, C, and HC to form H_2S and CH_4 are energetically highly demanding.

Cleavage of the first CS molecule does more than funnel reactivity toward H_2S and CH_2 fragments: It also generates surface carbon and sulfur adatoms that can engage in further coupling chemistry and form more complex species. We therefore examined the reactivity of a second CS molecule in the absence of H_2. In all cases, the starting configuration M in Figure 5 corresponds to a second CS adsorbed on Fe_{13}@CHA in the presence of the pre-existing carbon and sulfur moieties from the first CS scission. From M, three primary channels compete (intermediates N, O, and P in Figure 5). First, CS can couple with sulfur to form CS_2 (N). The corresponding pathway proceeds through a transition state with a barrier of 20.4 kcal mol^{-1} leading to the exergonic formation of N. Second, CS can couple with the carbon adatom to form C_2S (O), presenting a lower energy barrier of 11.9 kcal mol^{-1} and yielding a more exergonic product than N. Finally, the second CS molecule can also undergo C—S bond cleavage to form an additional pair of carbon and sulfur fragments (P). This pathway has a barrier of 10.4 kcal mol^{-1} and leads to the most exergonic product among the three. These energetics indicate strong competition between CS scission and C_2S formation (the barriers differ by only 1.5 kcal mol^{-1}), whereas CS_2 formation is less energetically favored. Once P is formed, the additional carbon and sulfur fragments can in principle undergo homocoupling. We therefore considered S—S coupling to form a disulfide-like unit S_2 and C—C coupling to form a C_2 fragment (Q and R, of Figure 5, respectively). S—S coupling displays a high barrier of 50.4 kcal mol^{-1} and yields an endergonic product Q, whereas C—C coupling proceeds with a much lower barrier of 9.4 kcal mol^{-1} and leads to an exergonic product R. These two processes thus do not effectively compete: under the present conditions, carbon–carbon bond formation is clearly preferred over sulfur–sulfur coupling. From a mechanistic standpoint, these additional pathways show that once CS scission has taken place, insertion of a second CS molecule (instead than H_2) can extend the reaction network toward C_xS_y-type and C_2-containing intermediates. This reinforces the view that Fe_{13}@CHA not only promotes C—S bond activation but can also catalyze the growth of more complex C/S frameworks under confinement.

3 | Discussion

The mechanistic analyses shown above disentangle the pathways and energetics of the processes studied. The initially hypothesized

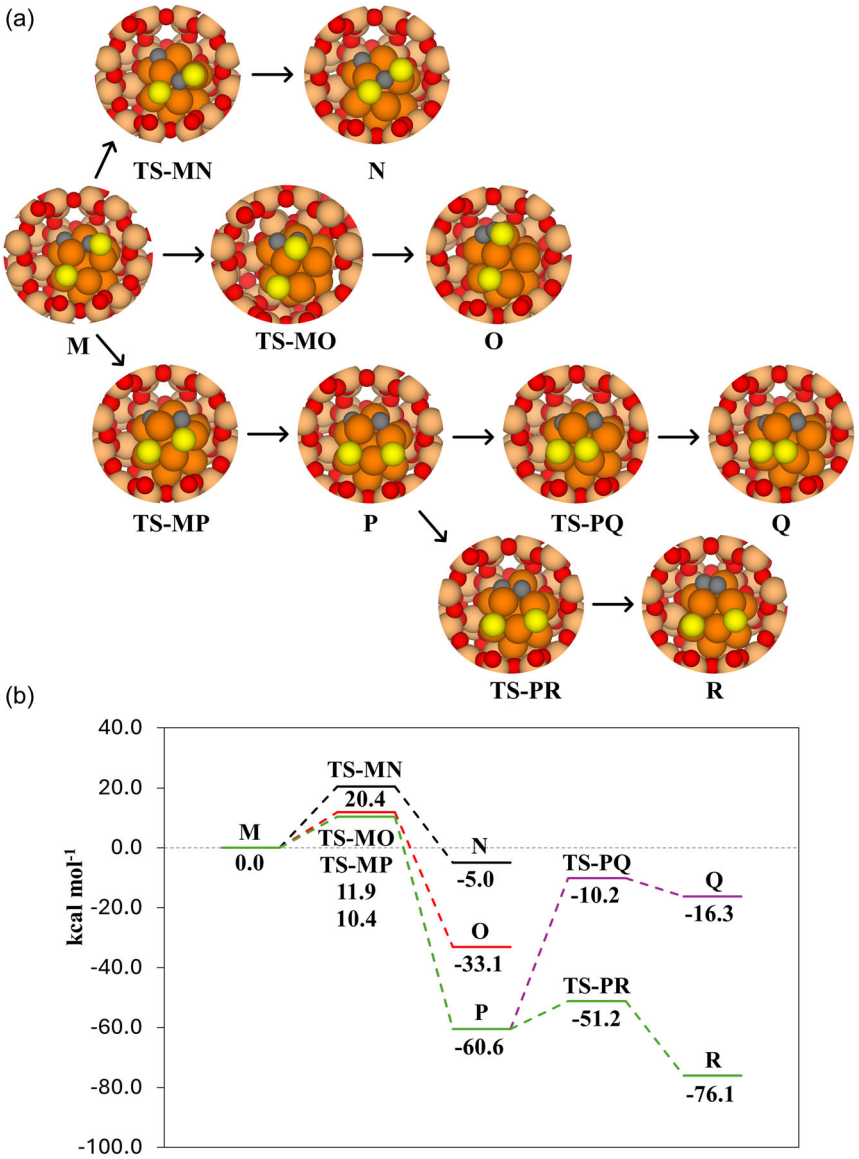

FIGURE 5 | (a) Optimized structures and transition state structures for the reaction processes of CS_2 formation, C_2S formation, second CS cleavage, S_2 formation, and C_2 formation. (b) Potential energy surface for the hydrogenation process. Energies are in kcal mol^{-1}. Color coding: white, H atoms; red, O atoms; beige, Si atoms; orange, Fe atoms; gray, C atoms; and yellow, S atoms.

route (H_2CS formation) is shown to be energetically unfeasible, in favor of the C—S bond cleavage, hence revealing hidden channels that bypass the prevailing hydrogenation product. To place these findings in an astrochemical context, mechanisms are complemented with (i) binding energies (BEs), which are informative for understanding the retention on the surface or release into the gas of the reactants, intermediates, and products (and hence determine whether the different reaction elementary steps follow each other appropriately), and (ii) kinetics, which provide an estimate of the temperature conditions in which the reactions are feasible in space.

3.1 | BEs

In astrochemistry, BEs govern surface retention of species on grain surfaces and, conversely, their release into the gas, thus influencing the observability of such species. Additionally, in terms of astrocatalysis, BEs also modulate catalytic turnover, with the following rule of thumb: BE too strong → poisoning; BE too weak → insufficient activation. Table 1 compiles the BEs for all the stable species considered in the set of reactions studied (i.e., reactants, intermediates, and products). Both H_2 (here as dissociated into two H adatoms) and CS bind strongly onto Fe_{13}@CHA. Upon C–S scission, the C and S adatoms bind even more strongly than CS (BE about 156 kcal mol^{-1} each). The first hydrogenation step differentiates the two possible paths (formation of either SH or CH): SH exhibits a markedly reduced BE (≈82 kcal mol^{-1}), still within the chemisorption regime, but weaker than CH (≈130 kcal mol^{-1}). This weaker SH BE compared to CH is translated into a higher S hydrogenation barrier compared to the C-hydrogenation one, as well as in the largely endergonic formation of HS (structure **F** of Figure 5) compared to the slightly endergonic formation of CH (structure **H** of Figure 6).

At the next step, H_2S shows a moderate reduction in BE relative to SH (35.2 kcal mol^{-1}), whereas CH_2 undergoes a substantial BE

TABLE 1 | Collected binding energies for all the molecules, intermediates, and products for the proposed reactions. Energies are in kcal mol^{-1}.

Molecule	BE
H_2	161.8
CS	147.7
S	155.9
C	156.8
HS	81.8
H_2S	35.2
CH	130.4
CH_2	62.4
CH_3	51.8
CH_4	27.0
Second CS	107.8
CS_2	125.5
C_2S	134.1
S_2	129.1
C_2	232.9

increase compared to CH (62.4 kcal mol^{-1}), this latter case explaining the high second barrier observed in C-hydrogenation. The CH_3 and CH_4 formation induces a reduction of their BEs (62.4 and 51.8 kcal mol^{-1}, respectively). Interestingly, both H_2S and CH_4 final products are those presenting the lowest BEs, which are the cases in which partial desorption from the surface could be observed.

Finally, a similar trend is observed for the second insertion of a CS molecule. Note that the BEs for the carbon and sulfur atoms are taken to be the same as those reported initially in Table 1. Remarkably, the second CS molecule shows a reduced BE compared with the first one. We attribute this to steric hindrance: The nanocluster is already partially occupied by the C and S adatoms, such that the second CS binds weaklier. Interestingly, the final C_2-containing product displays the largest BE among all the systems studied.

To sum up, BEs of the target species at the metal center indicate that most of them, especially CS, C, S, and C_2, are strongly chemisorbed. The pore-confined metal site can therefore act as a reservoir for S-bearing species. However, such strong adsorption has a second consequence: Whenever a reaction step entails weakening the metal–adsorbate interaction, part of the activation energy is spent on that detachment, and the corresponding barrier increases.

3.2 | Kinetics

Beyond BEs, kinetics constrain the astrophysical regimes where the investigated reactivity is feasible. In an astrophysical context, a rate constant of 1 yr^{-1} (i.e., one reaction per year) is generally regarded as the lower threshold for a reaction to be considered relatively fast on astronomical timescales, given that the typical age of a molecular cloud is about 10^6 years. Therefore, in our kinetic analysis, we identified the temperature at which each elementary step reaches $k = 1\,yr^{-1}$. Table 2 summarizes the kinetic results. For the initial steps, TS-CD (first hydrogenation to CS forming HCS) and TS-EF (C–S cleavage) have comparable barriers, the former slightly lower, corresponding to temperatures of ~230 and ~273 K at which $k \approx 1\,yr^{-1}$, respectively. These

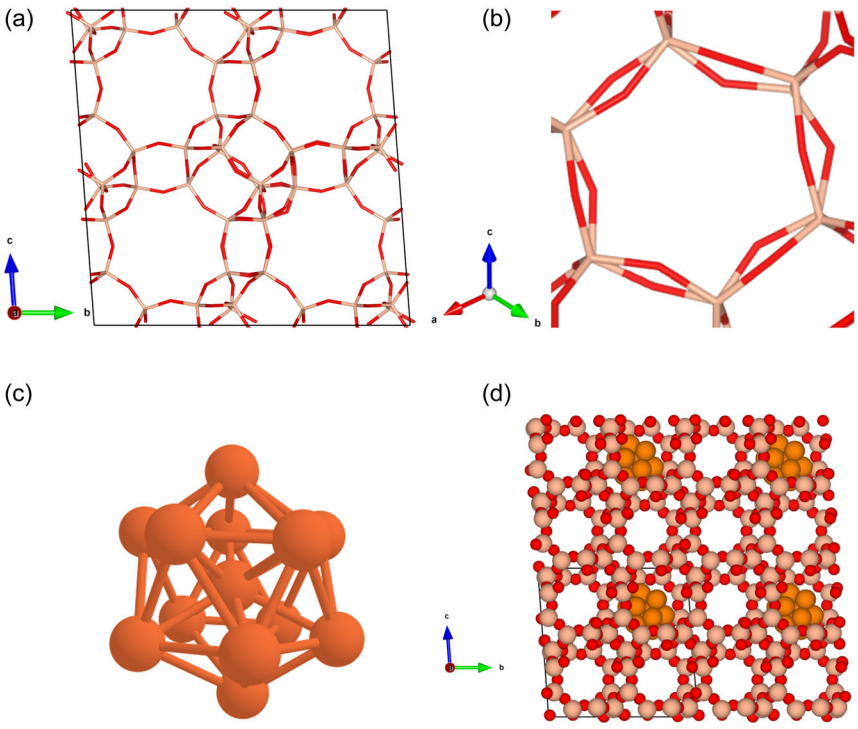

FIGURE 6 | (a) Optimized structure of the chabazite framework showing the eight-membered ring. (b) Zoom-in on the optimized structure of the chabazite framework showing the six-membered ring. (c) Optimized Fe_{13} structure before its introduction to chabazite. (d) Final optimized structure of the Fe_{13}@CHA. Color coding: white, H atoms; red, O atoms; beige, Si atoms; orange, Fe atoms; gray, C atoms; and yellow, S atoms.

TABLE 2 | Collected the rate constant (k) in years^{-1} (yr^{-1}), temperatures (T) in Kelvins (K), the relative energetic barrier ($\Delta U^{\ddagger}$), and the reaction energy (ΔU_{Rx}) in kcal mol^{-1} for all the reaction steps involving an energetic barrier studied in this work.

Reaction step		K, yr^{-1}	T, K	$\Delta U^{\ddagger}$	ΔU_{Rx}
CS hydrogenation	TS-CE	1.10	230	21.9	−15.1
C–S cleavage	TS-CD	1.05	273	24.7	−18.0
S hydrogenation	TS-EF	1.06	537	51.4	46.5
	TS-FG	1.26	171	15.7	−5.0
C hydrogenation	TS-EH	1.15	176	16.0	3.0
	TS-HI	1.05	448	40.0	−5.0
	TS-JK	1.06	451	42.1	17.3
	TS-KL	1.10	208	19.5	−16.9
CS_2 formation	TS-MN	1.01	212	20.4	−5.0
C_2S formation	TS-MO	1.15	123	11.9	−33.4
Second CS cleavage	TS-MP	1.28	115	10.4	−60.6
S_2 formation	TS-PQ	1.05	547	50.4	44.3
C_2 formation	TS-PR	1.46	120	11.3	−60.0

temperatures indicate that such processes operate preferentially in comparatively warm, evolved stages of planetary-system formation. For S hydrogenation, the first addition (HS) requires ∼537 K, whereas the second addition (H_2S) requires only ∼171 K, consistent with its much lower barrier. The hydrogenation of the C moiety also requires temperatures higher than 176 K, being the steps of CH_2 and CH_3 the most temperature demanding.

Finally, insertion of a second CS molecule leads to more reactive pathways. As discussed above, the corresponding activation barriers are smaller than those for hydrogenation of the C and S surface moieties, which translates into higher rate constants and thus lower onset temperatures, with the notable exception of S_2 formation. In particular, C_2-containing products (C_2S and C_2) become feasible at lower temperatures than CS_2 and S_2. Moreover, the cleavage of the second CS molecule is predicted to occur at lower temperatures than the first CS scission.

Kinetic data shed light on the feasibility of the reactions across broader astrophysical environments. The reported barriers and derived rate constants indicate that the processes are constrained to stages of planetary-system formation where mid-to-high temperatures are present, like the inner regions of protoplanetary discs. At the same time, the strong trapping of C and S at the Fe_{13}@CHA site suggests that zeolitic grains could act as latent reservoirs of sulfur-bearing species, even if the final products (H_2S, CH_4) are only efficiently formed in comparatively warm regions. Using zeolites as reactive scaffolds in astrochemistry is pioneering; the results here are therefore field-relevant, demonstrating how pore confinement shapes reactivity. Whereas CS + H_2 is often assumed to hydrogenate sequentially, confinement favors C—S bond cleavage, yielding C and S adatoms that can undergo distinct hydrogenation sequences to CH_x and SH_x intermediates and C_xS_y or carbon–sulfur allotropes if we consider the insertion of a subsequent CS molecule. Moreover, because both metal centers and organic molecules can be trapped within zeolitic pores, these materials are compelling candidates for reservoirs: They act as sponges for organics while the embedded metal cluster strengthens retention and activation.

Finally, the reactions studied must occur where sufficiently high temperatures are available. This is not a drawback: Zeolitic frameworks will predominantly be exposed to gas (able to trap and react target molecules) after ice mantles have sublimated, as well as within pebbles whose matrices are rich in silicates. In this sense, the availability of the material aligns with the thermal conditions required by the chemistry: a win–win scenario.

4 | Conclusions

We have analyzed the reaction energetics governing the reactivity between H_2 and CS under confinement conditions imposed by the chabazite (CHA) zeolite hosting a supported Fe_{13} nanocluster (Fe_{13}@CHA). Mechanistic mapping reveals a departure from the canonical astrochemical expectation: The prevailing hydrogenation path of CS → HCS → H_2CS is disfavored because the C—S bond cleaves after the first H_2 addition. The calculated barriers show strong competition between direct C—S scission and initial hydrogenation, which is followed by spontaneous C–S cleavage; in both cases, the net outcome is C—S bond breaking. Subsequent S- and C-centered hydrogenations (forming H_2S and CH_4) are feasible but face substantial activation barriers. The insertion of a second CS molecule opens additional reaction channels leading to either C_2S or CS_2, with C_2S formation being less energetically demanding. The second CS can also undergo C—S bond scission, generating additional C and S allotropes; notably, this second scission step is lower in energy than the first one. Overall, we find that carbon-based coupling products (C_2S and C_2 are significantly less energetically demanding than the corresponding S-containing couplings, thereby favoring the formation of hydrocarbon-like fragments over S—S bonded species.

BE trends support these observations. Reactants are strongly trapped at the metal center; after C–S cleavage, C and S bind even more strongly than CS. Hydrogenation of S weakens adsorption markedly: HS and then H_2S are progressively less coordinated, so part of the activation energy is effectively spent on detaching the adsorbate from the surface, explaining the high first S

hydrogenation barrier and the endergonic HS intermediate. For carbon, CH remains strongly bound (lower first barrier), but CH_2 and CH_3 exhibit a pronounced BE drop, consistent with the larger second and third barriers. Finally, formation of CH_4 shows a smaller barrier, a similar trend as observed in the formation of H_2S, meaning that the formation of the final closed-shell products, is less energy demanding than formation of the previous intermediates. In the scenario where a second CS molecule is adsorbed, the same trend is observed. Notably, the second CS molecule exhibits a reduced BE, whereas the final C_2 allotrope displays the largest BE of all species considered.

Kinetic analysis shows that, in general, the pathways are temperature-dependent, operating in comparatively warm regions such as inner protoplanetary discs. Rather than being a limitation, this matches environments where dust grains and silicate frameworks like chabazite are available and where ices have largely sublimated, enabling effective gas–Fe_{13}@CHA interactions and reactivity.

Overall, Fe_{13}@CHA catalysis demonstrates that confinement controls selectivity in space: The pore geometry biases CS toward cleavage over stepwise hydrogenation, in contrast to usual assumptions in less confined surfaces. In parallel, the cotrapping of metal clusters and organics enhances the reservoir function of zeolites, supporting their role as hosts for metal–organic chemistry relevant to prebiotic evolution in the interstellar and protoplanetary milieu. These results therefore support the idea that zeolite-like porous silicates, hosting embedded metal clusters, are not only promising nanoreactors but also potential reservoirs for immobilized sulfur in protoplanetary environments.

5 | Methodology

5.1 | Computational Details

All the calculations were performed adopting a periodic approach and using the CP2K package [43]. Characterization of the PESs requires determining the structures and the energetics of the stationary points. For geometry optimizations, the semilocal PBEsol functional was used [44], along with the Grimme's D3(BJ) correction to include dispersion forces [45]. A double-ζ basis set (DZVP-MOLOPT-SR-GTH Gaussian basis set) was adopted for all the atom types, combined with a cut-off energy of 500 Ry for the plane wave auxiliary basis set [43, 46]. The Goedecker–Teter–Hutter pseudopotentials [47] were used to describe core electrons, while a mixed Gaussian and plane-wave approach [48] was employed for valence electrons. The energies of the stationary points were refined by performing single-point calculations onto the PBEsol-optimized geometries at the hybrid B3LYP functional theory level [49, 50], with the D3(BJ) dispersion correction and using the triple-ζ (TZVP) basis set. Note that the auxiliary density matrix method [51, 52] was used for the exact exchange when performing calculations with hybrid functionals. The selection of B3LYP-D3(BJ) method for the energetic refinement was based on a consistent benchmarking study, reported in our previous work on Fe_{13}@SiO_2 [27]. In the aforementioned work, several functionals (PBE, B3LYP, PBE0, BHLYP, and ωB97X with TZVP and D3(BJ)) were compared against DLPNO–CCSD(T)/cc-pVDZ reference calculations for an Fe_7 cluster, using the triplet–singlet energy gap as a reference descriptor. B3LYP-D3(BJ) and PBE0-D3(BJ) showed the best performance, with relative errors per atom of 8.6% and 8.1%, respectively. B3LYP was ultimately chosen as the functional, as it had already been employed in our previous studies on astrocatalytic FTT reactions [24–29], demonstrating very good agreement with DLPNO-CCSD(T)/cc-pVDZ results, especially on the electronic description of the Fe nanocluster. Its use also facilitates consistent comparisons across related studies. Moreover, the B3LYP-D3(BJ)//PBEsol-D3(BJ) computational scheme proved to be a cost-effective approach for the systems and reactions investigated.

The climbing image nudged elastic band [53] technique implemented in CP2K[43] was used to search for transition states, which were also calculated at the B3LYP-D3(BJ)//PBEsol-D3(BJ) theory level. Energy barriers were calculated as follows:

$$\Delta E^{\ddagger} = E_{TS} - E_{GS} \tag{1}$$

$$\Delta U^{\ddagger} = \Delta E^{\ddagger} + \Delta ZPE \tag{2}$$

$$\Delta G_T^{\ddagger} = \Delta E^{\ddagger} + \Delta G_T \tag{3}$$

where $\Delta E^{\ddagger}$ stands for the potential energy barrier and E_{TS} and E_{GS} for the absolute potential energies of the transition states and the previous local minima, respectively; $\Delta U^{\ddagger}$ represents the zero-point energy (ZPE)-corrected barrier (in which ΔZPE refers to the contribution of the ZPE corrections to $\Delta E^{\ddagger}$); and $\Delta G_T^{\ddagger}$ for the Gibbs energy barrier at a given temperature, in which ΔG_T refers to the contribution of the Gibbs corrections to $\Delta E^{\ddagger}$.

The nature of the stationary points of the reactions was validated by calculating the harmonic frequencies (minima for reactants, intermediates, and products, and first-order saddle points showing only one imaginary frequency for transitions states). Vibrational harmonic frequencies were calculated at the PBEsol-D3BJ/DZVP-optimized structures using the finite differences method as implemented in the CP2K code [43]. To minimize the computational cost, the approximation to consider a partial Hessian matrix was employed. Consequently, vibrational frequencies were computed solely for a subset of the entire system, comprising the surface atoms participating in the reaction and the reactive species.

BEs have been computed at the B3LYP-D3(BJ)//PBEsol-D3(BJ) theory level and using the counterpoise method as implemented in CP2K to avoid basis set superposition error (BSSE). Final BSSE-corrected BEs were calculated as

$$\begin{aligned} \Delta E_{ads} &= E_{cplx} - (E_{sur} + E_m) \\ \Delta U_{ads} &= \Delta E_{ads} + \Delta ZPE \\ \Delta U_{ads} &= -BE \end{aligned} \tag{4}$$

where ΔE_{ads} is the potential adsorption energy; E_{cplx}, E_{sur}, and E_m are the absolute potential energies for the adsorption complex, the isolated surface, and the isolated molecule, respectively; ΔU_{ads} is the ZPE-corrected adsorption energy (in which ΔZPE refers to the contribution of the ZPE corrections to ΔE_{ads}); and BE is the binding energy (which is ΔU_{ads} in opposite sign).

The catalytic performance of the simulated reaction processes was investigated through reaction rate kinetic calculations. To this aim, a rate constant associated with each elementary barrier

was calculated using the Rice–Ramsperger–Kassel–Marcus (RRKM) theory [54], a microcanonical transition state theory that assumes that the phase space is statistically populated. In this RRKM treatment, tunneling effects were taken into account by adopting the unsymmetrical Eckart potential barrier model [55]. For the calculation of the rate constants, we used the calculated vibrational frequencies as degrees of freedom in the sum of states. Although we calculated a partial Hessian matrix to derive a set of vibrational modes, they are those directly involved in the reaction, and accordingly those that have a direct impact on the rate constants. The rest of the vibrational modes, which are not accounted for, belong to the zeolite bulk internal structure and are assumed to have a negligible influence in the chemical reactions and by extension the rate constants [56]. These kinetic calculations were performed with a freely available in-house program, in which the RRKM algorithms were implemented for grain-surface processes [57].

5.2 | Fe_{13}@CHA Model

The confinement scaffold is an all-silica chabazite (CHA), modeled as a fully 3D-periodic SiO_2 framework, the unit cell of which containing the $Si_{96}O_{192}$ unit (288 atoms, Figure 6a). Lattice and internal coordinates were fully optimized at the PBEsol level without symmetry constraints, yielding the following optimized unit cell parameters: $a = 18.54$ Å, $b = 18.63$ Å, and $c = 18.63$ Å and $\alpha = 93.83°$, $\beta = 94.47°$, and $\gamma = 94.78°$. Electronic sampling used Γ-point only due to the large real-space cell. The characteristic eight-membered ring (8MR, Figure 6b) aperture (∼3.8 Å) is retained after relaxation (minimum across-window O···O distances consistent with a ∼3.8 Å pore-limiting diameter), ensuring that the intrinsic size/shape constraints of CHA are preserved for the confined chemistry studied here.

A 13-atom iron nanocluster (Fe_{13}) is chosen (Figure 6c) as a representative Fe aggregation relevant to astrochemistry and for comparability with prior studies. Fe_{13} is a well-known magic-number cluster with enhanced stability [58, 59]. The cluster is treated as Fe^0 and described with an unrestricted spin formalism. Consistent with previous benchmarks, we employ a high-spin state with a total electronic multiplicity 27 ($S = 13$), approximately two unpaired electrons per Fe atom on average; alternative spin seeds were checked to confirm the ground-state manifold [27].

The Fe_{13} was inserted into a CHA cage and fully relaxed (Fe_{13}@CHA, Figure 6d). The confined cluster remains close to icosahedral, exhibiting moderate interfacial distortions. In the isolated Fe_{13}, Fe–Fe distances span 2.38–2.56 Å (average 2.41 Å), while in Fe_{13}@CHA, Fe–Fe distances broaden to 2.32–2.75 Å (average 2.46 Å), indicating local expansion/compression at the interface while largely preserving the icosahedral core. The dominant contacts are Fe···O-framework interactions to siloxane (Si–O–Si) oxygens of the cage and direct Fe–Si bonding.

Author Contributions

Albert Rimola: conceptualization (equal), formal analysis (equal), funding acquisition (lead), investigation (equal), project administration (lead), resources (lead), supervision (lead), writing – review and editing (lead). **Gerard Pareras:** conceptualization (lead), data curation (lead), formal analysis (lead), investigation (lead), methodology (lead), software (lead), validation (lead), visualization (lead), writing – original draft (lead).

Acknowledgments

A.R. acknowledges funding within the European Union's Horizon 2020 research and innovation program from the European Research Council (ERC) for the project Quantum Chemistry on Interstellar Grains (QUANTUMGRAIN), grant agreement No. 865657. A.R and G.P. acknowledge the European Union's Horizon Europe research and innovation program under the Marie Sklodowska-Curie grant agreement No. 101105235 for the funding of CHAOS project. G.P. thankfully acknowledges financial support by the Spanish Ministry of Universities and the European Union's Next Generation EU fund for a Margarita Salas contract. Spanish MICINN is also acknowledged for funding the projects PID2024-157971NB-C21 and CNS2023-144902. The authors thankfully acknowledge RES by BSC for the use of MareNostrum (activity QHS-2023-10019). The supercomputational facilities provided by CSUC are also acknowledged. The authors also acknowledge the EuroHPC Joint Undertaking through the Regular Access call project no. EU2025R01-014, hosted by the Ministry of Education, Youth and Sports of the Czech Republic through the e-INFRA CZ (ID: EU-25-91). A.R. acknowledges Accademia delle Scienze di Torino for supporting the project "In silico interstellar grain-surface chemistry". A.R. gratefully acknowledges support through 2023 ICREA Award.

Funding

This study was supported by H2020 European Research Council (865657), HORIZON EUROPE Marie Sklodowska-Curie Actions (101105235), and Ministerio de Ciencia e Innovación (CNS2023-144902, PID2024-157971NB-C21).

Conflicts of Interest

The authors declare no conflicts of interest.

Data Availability Statement

The data that support the findings of this study are available in the Supporting Information of this article.

References

1. J. Weitkamp, "Zeolites and Catalysis," *Solid State Ionics* 131 (2000): 175–188.

2. A. Corma, "Inorganic Solid Acids and Their Use in Acid-Catalyzed Hydrocarbon Reactions," *Chemical Reviews* 95 (1995): 559–614.

3. A. Corma, "State of the Art and Future Challenges of Zeolites as Catalysts," *Journal of Catalysis* 216 (2003): 298–312.

4. M. Król, "Natural vs. Synthetic zeolites," *Crystals* 10 (2020): 1–8.

5. T. Derbe, S. Temesgen, and M. Bitew, "A Short Review on Synthesis, Characterization, and Applications of Zeolites," *Advances in Materials Science and Engineering* 2021 (2021): 6637898.

6. S. Sonti, C. Sun, Z. Chen, et al., "Stability and Dynamics of Zeolite-Confined Gold Nanoclusters," *Journal of Chemical Theory and Computation* 11 (2024): 11.

7. M. Liu, C. Miao, and Z. Wu, "Recent Advances in the Synthesis, Characterization, and Catalytic Consequence of Metal Species Confined Within Zeolite for Hydrogen-Related Reactions," *Industrial Chemistry & Materials* 2 (2024): 57–84.

8. D. Z. Oehler and G. Etiope, "Methane Seepage on Mars: Where to Look and why," *Astrobiology* 17 (2017): 1233.

9. J. C. Viennet, B. Bultel, L. Riu, and S. C. Dioctahedral Werner, "Phyllosilicates Versus Zeolites and Carbonates Versus Zeolites Competitions as Constraints to Understanding Early Mars Alteration Conditions," *Journal of Geophysical Research: Planets* 122 (2017): 2328–2343.

10. S. W. Ruff, "Spectral Evidence for Zeolite in the Dust on Mars," *Icarus* 168 (2004): 131–143.

11. O. Mousis, J. M. Simon, J. P. Bellat, et al., "Martian Zeolites as a Source of Atmospheric Methane," *Icarus* 278 (2016): 1–6.

12. A. V. Rusol, "Porous Dust Clusters in Protoplanetary Disks as Catalysts for Formation of Complex Preorganic Compounds," *Solar System Research* 58 (2024): S40–S49.

13. V. Mouarrawis, R. Plessius, J. I. van der Vlugt, and J. N. H. Reek, "Confinement Effects in Catalysis Using Well-Defined Materials and Cages," *Frontiers in Chemistry* 6 (2018): 419863.

14. M. E. Potter, J. Amsler, L. Spiske, et al., "Combining Theoretical and Experimental Methods to Probe Confinement Within Microporous Solid Acid Catalysts for Alcohol Dehydration," *ACS Catalysis* 13 (2023): 5955–5968.

15. Q. Fang, Q. Sun, J. Ge, H. Wang, and J. Qi, "Multidimensional Engineering of Nanoconfined Catalysis: Frontiers in Carbon-Based Energy Conversion and Utilization," *Catalysts* 15 (2025): 477.

16. C. Bie, J. Yang, X. Zeng, et al., "Nanoconfinement Effects in Electrocatalysis and Photocatalysis," *Small* 21 (2025): 2411184.

17. A. Potapov, M. R. S. McCoustra, R. Tazaki, et al., "Is Cosmic Dust Porous?," *Astronomy and Astrophysics Review* 33 (2025): 6.

18. S. Zhukovska, T. Henning, and C. Dobbs, "Iron and Silicate Dust Growth in the Galactic Interstellar Medium: Clues from Element Depletions," *Astrophysical Journal* 857 (2018): 94.

19. I. Psaradaki, E. Costantini, D. Rogantini, et al., "Oxygen and Iron in Interstellar Dust: An X-Ray Investigation," *Astronomy and Astrophysics* 670 (2023): A30.

20. E. Dwek, "Iron: A Key Element for Understanding the Origin and Evolution of Interstellar Dust," *Astrophysical Journal* 825 (2016): 136.

21. E. B. Jenkins, "A Unified Representation of Gas-Phase Element Depletions in the Interstellar Medium," *Astrophysical Journal* 700 (2009): 1299–1348.

22. N. Kosinov, C. Liu, E. J. M. Hensen, and E. A. Pidko, "Engineering of Transition Metal Catalysts Confined in Zeolites," *Chemistry of Materials* 30 (2018): 3177–3198.

23. P. J. Smeets, J. S. Woertink, B. F. Sels, E. I. Solomon, and R. A. Schoonheydt, "Transition-Metal Ions in Zeolites: Coordination and Activation of Oxygen," *Inorganic Chemistry* 49 (2010): 3573–3583.

24. G. Pareras, V. Cabedo, M. McCoustra, and A. Rimola, "Single-Atom Catalysis in Space: Computational Exploration of Fischer- Tropsch Reactions in Astrophysical Environments," *Astronomy and Astrophysics* 680 (2023): A57.

25. G. Pareras, V. Cabedo, M. McCoustra, and A. Rimola, "Single-Atom Catalysis in Space-II. Ketene–acetaldehyde–ethanol and Methane Synthesis via Fischer-Tropsch Chain Growth," *Astronomy and Astrophysics* 687 (2024): A230.

26. G. Pareras and A. Rimola, "Single-Atom Iron on Silicon Carbide Surfaces as Catalyst of Fischer-Tropsch-Type Reactions in Astrophysical Environments," *Frontiers in Astronomy and Space Sciences* 12 (2025): 1605553.

27. G. Pareras, V. Cabedo, M. McCoustra, and A. Rimola, "Comprehensive Atomistic Simulations of Fischer-Tropsch in Outer Space: Astrocatalysis by Fe13-Supported Nanoclusters on SiO2," *Journal of Physical Chemistry C* 129 (2025): 10069–10082.

28. B. Martinez-Bachs, A. Anguera-Gonzalez, G. Pareras, and A. Rimola, "Formation of Methanol via Fischer-Tropsch Catalysis by Cosmic Iron Sulphide," *ChemPhysChem* 25 (2024): e202400272.

29. V. Cabedo, G. Pareras, J. Allitt, et al., "Reactivity of Chondritic Meteorites under H2-Rich Atmospheres: Formation of H2S," *Monthly Notices of the Royal Astronomical Society* 535 (2024): 2714–2723.

30. V. Cabedo, J. Llorca, J. M. Trigo-Rodriguez, and A. Rimola, "Study of Fischer-Tropsch-Type Reactions on Chondritic Meteorites," *Astronomy and Astrophysics* 650 (2021): A160.

31. P. Rivière-Marichalar, A. Fuente, J. R. Goicoechea, et al., "Abundances of Sulphur Molecules in the Horsehead Nebula: First NS+ Detection in a Photodissociation Region," *Astronomy and Astrophysics* 628 (2019): A16.

32. J. C. Howk, K. R. Sembach, and B. D. Savage, "A Method for Deriving Accurate Gas-Phase Abundances for the Multiphase Interstellar Galactic Halo," *Astrophysical Journal* 637 (2006): 333–341.

33. A. Herath, M. McAnally, A. M. Turner, et al., "Missing Interstellar Sulfur in Inventories of Polysulfanes and Molecular Octasulfur Crowns," *Nature Communications* 16 (2025): 5571.

34. X. J. Yang, L. Hua, and A. Li, "Where Have All the Sulfur Atoms Gone? Polycyclic Aromatic Hydrocarbon as a Possible Sink for the Missing Sulfur in the Interstellar Medium. I. The C–S Band Strengths," *Astrophysical Journal* 974 (2024): 30.

35. D. A. Neufeld, B. Godard, M. Gerin, et al., "Sulphur-Bearing Molecules in Diffuse Molecular Clouds: New Results from SOFIA/GREAT and the IRAM. 30 m Telescope," *Astronomy and Astrophysics* 577 (2015): A49.

36. A. Tieftrunk, G. Pineau des Forets, P. Schilke, and C. M. Walmsley, "SO and H2S in Low Density Molecular Clouds," *Astronomy and Astrophysics* 289 (1994): 579–596.

37. C. Vastel, D. Quénard, R. Le Gal, et al., "Sulphur Chemistry in the L1544 Pre-Stellar Core," *Monthly Notices of the Royal Astronomical Society* 478 (2018): 5519–5537.

38. V. Wakelam, A. Castets, C. Ceccarelli, B. Lefloch, E. Caux, and L. Pagani, "Sulphur-Bearing Species in the Star Forming Region L1689N," *Astronomy and Astrophysics* 413 (2004): 609–622.

39. T. H. G. Vidal, J. C. Loison, A. Y. Jaziri, M. Ruaud, P. Gratier, and V. Wakelam, "On the Reservoir of Sulphur in Dark Clouds: Chemistry and Elemental Abundance Reconciled," *Monthly Notices of the Royal Astronomical Society* 469 (2017): 435–447.

40. J. C. Laas and P. Caselli, "Modeling Sulfur Depletion in Interstellar Clouds," *Astronomy and Astrophysics* 624 (2019): A108.

41. D. P. Ruffle, T. W. Hartquist, P. Caselli, and D. A. Williams, "The Sulphur Depletion Problem," *Monthly Notices of the Royal Astronomical Society* 306 (1999): 691–695.

42. T. J. Millar and E. Herbst, "Organo-Sulphur Chemistry in Dense Interstellar Clouds," *Astronomy and Astrophysics* 231 (1990): 466–472.

43. T. D. Kühne, M. Iannuzzi, M. Del Ben, et al., "CP2K: An Electronic Structure and Molecular Dynamics Software Package -Quickstep: Efficient and Accurate Electronic Structure Calculations," *Journal of Chemical Physics* 152 (2020): 194103.

44. J. P. Perdew, A. Ruzsinszky, G. I. Csonka, et al., "Restoring the Density-Gradient Expansion for Exchange in Solids and Surfaces," *Physical Review Letters* 100 (2008): 136406.

45. S. Grimme, J. Antony, S. Ehrlich, and H. Krieg, "A Consistent and Accurate Ab Initio Parametrization of Density Functional Dispersion Correction (DFT-D) for the 94 Elements H-Pu," *Journal of Chemical Physics* 132 (2010): 154104.

46. J. Vandevondele, M. Krack, F. Mohamed, M. Parrinello, T. Chassaing, and J. Hutter, "Quickstep: Fast and Accurate Density Functional Calculations Using a Mixed Gaussian and Plane Waves Approach," *Computer Physics Communications* 167 (2005): 103–128.

47. S. Goedecker and M. Teter, "Separable Dual-Space Gaussian Pseudopotentials," *Physical Review B: Condensed Matter* 54 (1996): 1703–1710.

48. G. Lippert, J. Hutter, and M. Parrinello, "A Hybrid Gaussian and Plane Wave Density Functional Scheme," *Molecular Physics* 92 (1997): 477–488.

49. A. D. Becke, "A New Mixing of Hartree-Fock and Local Density-Functional Theories," *Journal of Chemical Physics* 98 (1993): 1372–1377.

50. C. Lee, W. Yang, and R. G. Parr, "Development of the Colle-Salvetti Correlation-Energy Formula into a Functional of the Electron Density," *Physical Review B* 37 (1988): 785–789.

51. M. Guidon, J. Hutter, and J. VandeVondele, "Robust Periodic Hartree-Fock Exchange for Large-Scale Simulations Using Gaussian Basis Sets," *Journal of Chemical Theory and Computation* 5 (2009): 3010–3021.

52. M. Guidon, J. Hutter, and J. Vandevondele, "Auxiliary Density Matrix Methods for Hartree-Fock Exchange Calculations," *Journal of Chemical Theory and Computation* 6 (2010): 2348–2364.

53. N. A. Zarkevich and D. D. Johnson, "Nudged-Elastic Band Method with Two Climbing Images: Finding Transition States in Complex Energy Landscapes," *Journal of Chemical Physics* 142 (2015): 24106.

54. R. A. Marcus, "Unimolecular Dissociations and Free Radical Recombination Reactions," *Journal of Chemical Physics* 20 (1952): 359–364.

55. C. Eckart, "The Penetration of a Potential Barrier by Electrons," *Physical Review* 35 (1930): 1303–1309.

56. G. Molpeceres, V. Zaverkin, K. Furuya, Y. Aikawa, and J. Kästner, "Reaction Dynamics on Amorphous Solid Water Surfaces Using Interatomic Machine-Learned Potentials: Microscopic Energy Partition Revealed from the P + H → PH Reaction," *Astronomy and Astrophysics* 673 (2023): A51.

57. J. Enrique-Romero, and A. Rimola, *QuantumGrain RRKM code*, (2022), https://doi.org/10.5281/ZENODO.10518616.

58. A. S. Chaves, M. J. Piotrowski, and J. L. F. Da Silva, "Evolution of the Structural, Energetic, and Electronic Properties of the 3d, 4d, and 5d Transition-Metal Clusters (30 TMn Systems for n = 2-15): A Density Functional Theory Investigation," *Physical Chemistry Chemical Physics* 19 (2017): 15484–15502.

59. S. Gueddida, M. Badawi, and S. Lebègue, "Grafting of Iron on Amorphous Silica Surfaces from Ab Initio Calculations," *Journal of Chemical Physics* 152 (2020): 214706.

Supporting Information

Additional supporting information can be found online in the Supporting Information section. The supporting information includes the data obtained from the preliminary results for the $Fe_{13}@SiO_2$ catalyst, and all the computational data including all the relative energies at both levels of theory (PBEsol and B3LYP) as well as with zero-point and Gibbs energy corrections. Benchmarking for the partial Hessian Matrix approach. Description of the RRKM theory employed in the article. **Supporting Fig. S1:** Optimized structure for the $Fe_{13}@SiO_2$ + H + HCS intermediate. Also depicted HC–S distance in Angstroms (Å). Color coding: white, H atoms; red, O atoms; beige, Si atoms; orange, Fe atoms; gray, C atoms; and yellow, S atoms. **Supporting Table S1:** Collected the relative energies in kcal mol^{-1} for the processes of hydrogenation of CS and C–S scission on the $Fe_{13}@SiO_2$ catalyst. **Supporting Table S2:** Relative energies (in kcal mol^{-1}) for the CS hydrogenation reaction pathway: relative potential energies (ΔE) at the PBEsol-D3(BJ) and B3LYP-D3(BJ)//PBEsol-D3(BJ)levels of theory, relative zero-point energy-corrected energies (ΔU), and Gibbs energies (ΔG) at 200, 400, and 600 K, calculated at the B3LYP-D3(BJ)//PBEsol-D3(BJ) level of theory. **Supporting Table S3:** Relative energies (in kcal mol^{-1}) for the CS scission reaction pathway: relative potential energies (ΔE) at the PBEsol-D3(BJ) and B3LYP-D3(BJ)//PBEsol-D3(BJ)levels of theory and relative zero-point energy-corrected energies (ΔU), and Gibbs energies (ΔG) at 200, 400, and 600 K, calculated at the B3LYP-D3(BJ)//PBEsol-D3(BJ) level of theory. **Supporting Table S4:** Relative energies (in kcal mol^{-1}) for the H_2S formation reaction pathway: relative potential energies (ΔE) at the PBEsol-D3(BJ) and B3LYP-D3(BJ)//PBEsol-D3(BJ) levels of theory, relative zero-point energy-corrected energies (ΔU), and Gibbs energies (ΔG) at 200, 400, and 600 K, calculated at the B3LYP-D3(BJ)//PBEsol-D3(BJ) level of theory. **Supporting Table S5:** Relative energies (in kcal mol^{-1}) for the CH_4 formation reaction pathway: relative potential energies (ΔE) at the PBEsol-D3(BJ) and B3LYP-D3(BJ)//PBEsol-D3(BJ)levels of theory, relative zero-point energy-corrected energies (ΔU), and Gibbs energies (ΔG) at 200, 400, and 600 K, calculated at the B3LYP-D3(BJ)//PBEsol-D3(BJ) level of theory. **Supporting Table S6:** Relative energies (in kcal mol^{-1}) for the CS_2 formation reaction pathway: relative potential energies (ΔE) at the PBEsol-D3(BJ) and B3LYP-D3(BJ)//PBEsol-D3(BJ)levels of theory, relative zero-point energy-corrected energies (ΔU), and Gibbs energies (ΔG) at 200, 400, and 600 K, calculated at the B3LYP-D3(BJ)//PBEsol-D3(BJ) level of theory. **Supporting Table S7:** Relative energies (in kcal mol^{-1}) for the CCS formation reaction pathway: relative potential energies (ΔE) at the PBEsol-D3(BJ) and B3LYP-D3(BJ)//PBEsol-D3(BJ)levels of theory, relative zero-point energy-corrected energies (ΔU), and Gibbs energies (ΔG) at 200, 400, and 600 K, calculated at the B3LYP-D3(BJ)//PBEsol-D3(BJ) level of theory. **Supporting Table S8:** Relative energies (in kcal mol^{-1}) for the CC formation reaction pathway: relative potential energies (ΔE) at the PBEsol-D3(BJ) and B3LYP-D3(BJ)//PBEsol-D3(BJ)levels of theory, relative zero-point energy-corrected energies (ΔU), and Gibbs energies (ΔG) at 200, 400, and 600 K, calculated at the B3LYP-D3(BJ)//PBEsol-D3(BJ) level of theory. **Supporting Table S9:** Relative energies (in kcal mol^{-1}) for the SS formation reaction pathway: relative potential energies (ΔE) at the PBEsol-D3(BJ) and B3LYP-D3(BJ)//PBEsol-D3(BJ)levels of theory, relative zero-point energy-corrected energies (ΔU), and Gibbs energies (ΔG) at 200, 400, and 600 K, calculated at the B3LYP-D3(BJ)//PBEsol-D3(BJ) level of theory. **Supporting Table S10**: Relative energies in kcal mol^{-1} for the CS scission step. The reported ΔU, $\Delta G_{(200)}$, $\Delta G_{(400)}$, and $\Delta G_{(600)}$ are calculated including 17 atoms in the Hessian matrix. **Supporting Table S11:** Relative energies in kcal mol^{-1} for the CS scission step. The reported ΔU, $\Delta G_{(200)}$, $\Delta G_{(400)}$, and $\Delta G_{(600)}$ are calculated including 27 atoms in the Hessian matrix. **Supporting Table S12:** Relative energies in kcal mol^{-1} for the CS scission step. The reported ΔU, $\Delta G_{(200)}$, $\Delta G_{(400)}$, and $\Delta G_{(600)}$ are calculated including 37 atoms in the Hessian matrix. **Supporting Table S13:** Relative energies in kcal mol^{-1} for the CS scission step. The reported ΔU, $\Delta G_{(200)}$, $\Delta G_{(400)}$, and $\Delta G_{(600)}$ are calculated including 47 atoms in the Hessian matrix. **Supporting Table S14:** Relative energies in kcal mol^{-1} for the CS scission step. The reported ΔU, $\Delta G_{(200)}$, $\Delta G_{(400)}$, and $\Delta G_{(600)}$ are calculated including 47 atoms in the Hessian matrix. **Supporting Table S15:** Calculated relative errors (Rel. Error) for each relative energy for the ΔU, $\Delta G_{(200)}$, $\Delta G_{(400)}$, and $\Delta G_{(600)}$ energies and for each number of atoms included in the Hessian matrix in the vibrational calculation. **Supporting Table S16:** Calculated relative errors (Rel. Error) for each relative energy for the ΔU, $\Delta G_{(200)}$, $\Delta G_{(400)}$, and $\Delta G_{(600)}$ energies and for each number of atoms included in the Hessian matrix in the vibrational calculation.